

OPEN ACCESS

Analysis and Simulation of One-Dimensional Transport Models for Lithium Symmetric Cells

To cite this article: Akshay Subramaniam *et al* 2019 *J. Electrochem. Soc.* **166** A3806

View the [article online](#) for updates and enhancements.



Analysis and Simulation of One-Dimensional Transport Models for Lithium Symmetric Cells

Akshay Subramaniam,^{1,*,*} Jerry Chen,^{1,*,*} Taejin Jang,^{2,*} Natalie R. Geise,³
Robert M. Kasse,⁴ Michael F. Toney,⁵ and Venkat R. Subramanian^{1,2,6,*,*,z}

¹Department of Chemical Engineering, University of Washington, Seattle, Washington 98195, USA

²Materials Science and Engineering Program, Texas Materials Institute, The University of Texas at Austin, Austin, Texas 78712, USA

³Department of Chemistry, Stanford University, California 94305, USA

⁴Department of Materials Science and Engineering, Stanford University, California 94305, USA

⁵SLAC National Accelerator Laboratory, California 94025, USA

⁶Department of Mechanical Engineering, Texas Materials Institute, The University of Texas at Austin, Austin, Texas 78712, USA

The main objective of this paper is to analyze transport models for lithium symmetric cells and arrive at an efficient model and code to simulate the same. Two one-dimensional models are considered. The first model uses the dilute solution Nernst–Planck equations in conjunction with the electroneutrality assumption (EN-NP model). For binary electrolytes, an analytical solution for electrolyte concentration is derived and compared with numerical solutions by an approximate finite volume method. The second approach relaxes the electroneutrality assumption by way of Poisson's equation for the electrostatic potential (PNP model). The computational difficulties of the PNP model are tackled using the approximate finite volume method, with demonstrated convergence characteristics even with bulk dimensions several orders of magnitude larger than the characteristic double layer size. A robust code is developed for the PNP model. The computationally efficient transport models can facilitate simulations, physical understanding, and analysis. This is illustrated by a case study in which these models are coupled with modified kinetic models, which are then parameterized with experimental voltage response data using a systems-level approach. The estimated parameters provide further insight into the electrochemical phenomena underpinning voltage transitions in symmetric cells.

© The Author(s) 2019. Published by ECS. This is an open access article distributed under the terms of the Creative Commons Attribution Non-Commercial No Derivatives 4.0 License (CC BY-NC-ND, <http://creativecommons.org/licenses/by-nc-nd/4.0/>), which permits non-commercial reuse, distribution, and reproduction in any medium, provided the original work is not changed in any way and is properly cited. For permission for commercial reuse, please email: oa@electrochem.org. [DOI: 10.1149/2.0261915jes]



Manuscript submitted May 13, 2019; revised manuscript received August 29, 2019. Published November 15, 2019. This was Paper 510 presented at the Cancun, Mexico, Meeting of the Society, September 30–October 4, 2018.

There is significant interest in lithium metal anodes to increase the energy density of lithium batteries, and thus achieve the metrics required to hasten the progress of electric transportation and grid-scale energy storage.¹ Lithium is highly electropositive, and lithium anodes have a higher theoretical specific capacity (3860 mAh·g⁻¹) compared to the graphite (372 mAh·g⁻¹) used in lithium-ion batteries.² Several failure modes and performance limitations hinder wider adoption, including low coulombic efficiency, reduced cycle life, and potentially unsafe internal short circuits during operation. These issues are a result of the high reactivity, large volume changes, and poor electrodeposition properties of lithium, characterized by parasitic side reactions, dendrite formation, inactive lithium, and other undesirable deposition phenomena.^{3–5} Obtaining a sound understanding of the interrelated ion transport phenomena in the electrolyte, and the lithium stripping and deposition kinetics at the electrodes is essential to investigate and prevent these issues in lithium metal batteries. Symmetric cells represent a convenient system for this purpose. Instead of studying the lithium anode in a full cell configuration, they consist of identical materials for both electrodes (Figure 1).⁶ This enables the study of lithium anode operation and electrodeposition dynamics sans compound interactions with other cell components. Symmetric cells are also useful for the evaluation of new electrolytes, additives, and separator materials. They can also be used in experiments for property measurements and electrochemical model validation.^{7,8}

Continuum-scale physics-based models can provide useful mechanistic insight grounded in electrochemical transport and kinetics, thus serving as a framework for the analysis and interpretation of symmetric cell data. The value of monitoring and correlating the cell voltage response with trends in deposition phenomena and internal electrochemistry has also been highlighted.^{5,9} In this regard, modeling per-

forms an important complementary function. Wood et al. used an one-dimensional (1-D) Poisson and Nernst–Planck (PNP) combined with a lumped electrode kinetics model to predict ion transport behavior and voltage response in a lithium symmetric cell, analyzing deposition and stripping trends.⁹ However, the paper also noted the difficulty in obtaining the desired numerical convergence at reasonable computational cost with classic finite difference methods (FDM). The choice of the computational scheme used for PNP-type models can greatly limit the utility of physics-based models in extended cycling simulations for aging studies or parameter estimation. Efficient and elegant solutions of the bulk ion transport equations greatly simplify the coupling of kinetic models to ultimately predict cell-level voltage response. This entails the careful consideration of the computational aspects of these models in order to determine the optimal simulation method.

Two common transport models for charged species transport, based on the Nernst–Planck flux laws, are Poisson and Nernst–Planck (PNP) equations and the Electroneutrality and Nernst–Planck (EN-NP) equations. These models chiefly differ in the form of the charge conservation laws. Although the PNP model is the more complete treatment of charged species transport and better describes transitions in the boundary layers near electrodes (typically 1 ~ 10 nm), obtaining the desired numerical convergence is non-trivial due to the very large coefficients (6.8×10^{14}) resulting from the $F/\epsilon_0\epsilon_s$ factor in Poisson's equation, where F is Faraday's constant (96485 C/mol), ϵ_0 is the vacuum permittivity (8.85×10^{-12} A²s²/Nm²), and ϵ_s represents the dielectric constant of the solvent (~15 for a typical organic solvent). These factors necessitate the use of appropriate dimensionless groups, scaling factors, and numerical discretization schemes.

The literature on the computational aspects of the PNP equations is extensive, beginning with the work of Cohen and Cooley, and that of Brumleve and Buck.^{10,11} Modified finite difference schemes have been employed for spatial discretization, with various implicit and semi-implicit schemes used for time integration.^{12–16} Spectral methods have also been exploited to achieve improved resolution of double layers for certain steady-state problems.^{17,18} In addition, some researchers have

^{*}These authors contributed equally to this work.

^{*}Electrochemical Society Student Member.

^{**}Electrochemical Society Fellow.

^zE-mail: venkat.subramanian@utexas.edu

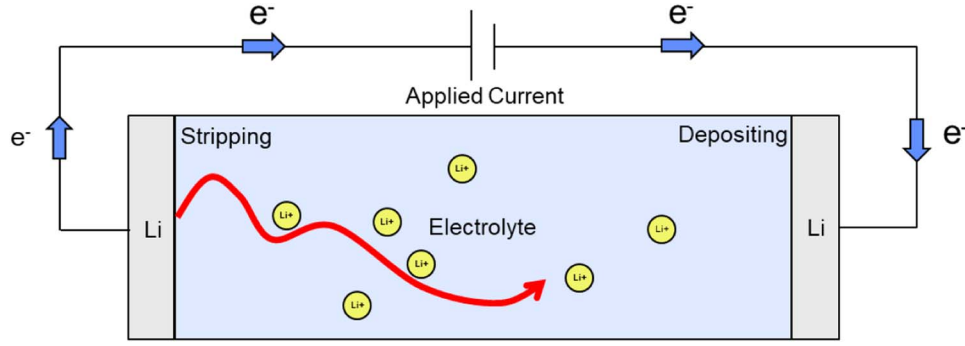


Figure 1. Schematic of a lithium symmetric cell.

attempted to find analytical solutions. Golovnev¹⁹ found the analytical form of PNP solutions in the linear regime under applied direct current. Pabst²⁰ also derived the analytical solution of the PNP equations for a system close to electroneutrality by introducing two different time constants. Analytical solutions for PNP can only be found under specific operating conditions and limiting assumptions.

In this study, we present an analytical solution for the concentration profiles in the EN-NP case. Using bulk electroneutrality is a common simplification in battery modeling, for example, in the porous electrode pseudo-two-dimensional (P2D) models of Newman and co-workers.^{21,22} We then present finite volume method (FVM) numerical schemes for dimensionless forms of both EN-NP and PNP models for a binary electrolyte. Furthermore, we compare EN-NP with PNP for galvanostatic operating conditions and the typical length and time scales encountered in lithium symmetric cells. In summary, we can use the FVM scheme to solve PNP and EN-NP models efficiently in a robust manner. For typical design parameters, we can further approximate PNP with EN-NP, leveraging the easy implementation of analytical solutions for the concentration profile to enhance simulation efficiency.

1-D Nernst-Planck System for Binary Electrolytes

Assuming a symmetric binary electrolyte with a constant diffusivity completely dissociating in a non-ionized solvent in the presence of uncharged background components, the 1-D Nernst-Planck²² constitutive relations can be used in species conservation laws, which consider transport in the absence of chemical reactions. For a common electrolyte ion pair, such as Li^+ and PF_6^- , these conservation equations can be written as:

$$\frac{\partial c_1}{\partial t} = -\frac{\partial N_1}{\partial x} \quad [1]$$

$$\frac{\partial c_2}{\partial t} = -\frac{\partial N_2}{\partial x} \quad [2]$$

where c is the concentration (mol/m^3), t is the time (s), N represents the total flux ($\text{mol}/\text{m}^2 \text{ s}$), and x is the position along the cell (m). For convenience, subscript 1 represents Li^+ and 2 denotes PF_6^- .

In the absence of convection, the Nernst-Planck (NP) constitutive equations for the fluxes are given by

$$N_1 = -D_1 \frac{\partial c_1}{\partial x} - z_1 c_1 u_1 F \frac{\partial \phi}{\partial x} \quad [3]$$

$$N_2 = -D_2 \frac{\partial c_2}{\partial x} - z_2 c_2 u_2 F \frac{\partial \phi}{\partial x} \quad [4]$$

where D is the diffusivity (m^2/s), z is the electric charge of the ion, u is the ionic mobility ($\text{mol}^2/\text{J s}$), F is the Faraday's constant (96485 C/mol), and ϕ is the mean-field electrostatic potential (V).

In the equation, the first term (diffusive flux) denotes the diffusion contribution due to the concentration gradient, and the second term represents the migration of charged ions under an electric field. u is the ionic mobility, which is the average migration velocity of the

species under a unit electric field, and zF is charge per mole of the species. In the dilute solution formulation, ion-ion interactions are neglected. A description based on the 'Onsager-Stefan-Maxwell' (OSM) flux laws will consider the complete set of pairwise interactions for all species.^{22,23} However, the computational methods outlined herein are applicable to the full OSM equations as well. In particular, for electroneutral systems comprising a binary electrolyte, both the EN-NP and the OSM equations reduce to a similar mathematical form, indicating direct extensibility to the mathematical treatment of concentrated binary electrolytes.

We can further link the ionic mobility (u) and diffusivity (D) by the Nernst-Einstein relation

$$u_1 = \frac{D_1}{RT} \quad [5]$$

$$u_2 = \frac{D_2}{RT} \quad [6]$$

where R is the gas constant (8.314 J/mol K), and T is the absolute temperature (K).

Hence, the mass transport equations can be written as:

$$\frac{\partial c_1}{\partial t} = -\frac{\partial}{\partial x} \left(-D_1 \frac{\partial c_1}{\partial x} - z_1 c_1 \frac{D_1 F}{RT} \frac{\partial \phi}{\partial x} \right) \quad [7]$$

$$\frac{\partial c_2}{\partial t} = -\frac{\partial}{\partial x} \left(-D_2 \frac{\partial c_2}{\partial x} - z_2 c_2 \frac{D_2 F}{RT} \frac{\partial \phi}{\partial x} \right) \quad [8]$$

The flux of the electroactive Li^+ species is related to the applied current density. The negatively charged PF_6^- ions are assumed not to react at either electrode. In the following sections, we will present solutions for the ion concentration and electrostatic potential profiles, beginning with EN-NP. The boundary conditions for both species are listed in Table I. The boundary conditions for all the species in our model are specified in terms of the normal component of their fluxes at each electrode.

Electroneutrality and Nernst-Planck (EN-NP)

Electroneutrality is generally an accurate assumption except in the 1–10 nm charged interfacial double layer region. Although the Poisson's equation (Equation 46) in PNP describes a system with a uniform dielectric constant more accurately than EN-NP, the presence of thin double layers with respect to characteristic system dimensions poses both modeling and computational challenges.²⁴ For the symmetric cell modeled here, this quantity, given by the ratio of the characteristic

Table I. Boundary conditions for Nernst-Planck equations.

I	Species	$x = 0$	$x = L$
1	Li^+	$N_1 _{x=0} = \frac{I_{app}}{z_1 F}$	$N_1 _{x=L} = \frac{I_{app}}{z_1 F}$
2	PF_6^-	$N_2 _{x=0} = 0$	$N_2 _{x=L} = 0$

Debye length to the characteristic system dimension, ϵ , is of the order of 10^{-7} . In general, EN-NP is substantially easier to solve numerically compared to the PNP system. Coupled with the increasing validity of the EN approximation as $\epsilon \rightarrow 0$, this motivates the use of the electroneutrality assumption to avoid the computational difficulties associated with thin boundary layers.^{15,25} Chu and Bazant¹⁷ commented that Levich²⁶ was probably the first to notice that the assumption of bulk electroneutrality yields approximate solutions to the Poisson-Nernst-Planck (PNP) equations. Additionally, the double layer structure at the electrode interface can often be implicitly considered in the boundary conditions.²² The electroneutrality condition is expressed as:

$$\sum_i z_i c_i = 0 \quad [9]$$

where z_i represents the charge of each ion and c_i represents the concentration of each ion species.

For a binary electrolyte, the electroneutrality relation provides:

$$z_1 c_1 + z_2 c_2 = 0 \quad [10]$$

Under this assumption, we obtain $c_1 = c_2$ and we can further define them as c when $z_1 = 1$ and $z_2 = -1$. Therefore, we can get the Nernst-Planck equations for both species from Equations 7 and 8.

$$\frac{\partial c}{\partial t} = -\frac{\partial}{\partial x} \left(-D_1 \frac{\partial c}{\partial x} - c \frac{D_1 F}{RT} \frac{\partial \phi}{\partial x} \right) \quad [11]$$

$$\frac{\partial c}{\partial t} = -\frac{\partial}{\partial x} \left(-D_2 \frac{\partial c}{\partial x} + c \frac{D_2 F}{RT} \frac{\partial \phi}{\partial x} \right) \quad [12]$$

During galvanostatic operation, the constant current density (I_{app}) can be related to the species fluxes as:

$$F \sum_i z_i N_i = F (z_1 N_1 + z_2 N_2) = I_{app} \quad [13]$$

In this case, we have:

$$F \left(\left(-D_1 \frac{\partial c}{\partial x} - c \frac{D_1 F}{RT} \frac{\partial \phi}{\partial x} \right) - \left(-D_2 \frac{\partial c}{\partial x} + c \frac{D_2 F}{RT} \frac{\partial \phi}{\partial x} \right) \right) = I_{app} \quad [14]$$

Therefore, from Equation 14, we can get:

$$\frac{\partial \phi}{\partial x} = \frac{RT}{cF} \left(\frac{D_2 - D_1}{D_1 + D_2} \right) \frac{\partial c}{\partial x} - \frac{RT}{cF^2} \left(\frac{I_{app}}{D_1 + D_2} \right) \quad [15]$$

If we substitute Equation 15 back into Equation 11, we can get:

$$\frac{\partial c}{\partial t} = \left(\frac{2D_1 D_2}{D_1 + D_2} \right) \frac{\partial^2 c}{\partial x^2} = D \frac{\partial^2 c}{\partial x^2} \quad [16]$$

where D can be defined as a binary electrolyte diffusivity:

$$D = \frac{2D_1 D_2}{D_1 + D_2} \quad [17]$$

We introduce the following dimensionless variables:

$$C = \frac{c}{c_0}, \quad X = \frac{x}{L}, \quad \tau = \frac{D}{L^2} t, \quad \text{and} \quad \delta = \frac{I_{app} L}{F c_0 D_1} \quad [18]$$

The governing equation in Equation 16, boundary conditions in Table I and initial conditions become:

$$\frac{\partial C}{\partial \tau} = \frac{\partial^2 C}{\partial X^2} \quad [19]$$

$$C(X, 0) = 1 \quad [20]$$

$$\frac{\partial C}{\partial X}(0, \tau) = -\frac{\delta}{2} \quad [21]$$

$$\frac{\partial C}{\partial X}(1, \tau) = -\frac{\delta}{2} \quad [22]$$

The dimensionless governing equation for electrolyte concentration is essentially a parabolic partial differential equation (PDE) with two non-homogenous flux boundary conditions.

Analytical solution of EN-NP model.—We obtain an analytical solution for $C(X, \tau)$ using the separation of variables (SOV) approach.²⁷ First, we assume the form of the solution as follows:

$$C(X, \tau) = g(X, \tau) + w(X) \quad [23]$$

In Equation 23, $g(X, \tau)$ satisfies the homogeneous part of boundary conditions, while $w(X)$ satisfies the non-homogeneous part.²⁸

The boundary conditions are therefore expressed as:

$$\frac{\partial g}{\partial X}(0, \tau) = 0, \quad \text{and} \quad \frac{\partial g}{\partial X}(1, \tau) = 0 \quad [24]$$

$$\frac{dw}{dX}(0) = -\frac{\delta}{2}, \quad \text{and} \quad \frac{dw}{dX}(1) = -\frac{\delta}{2} \quad [25]$$

By substituting Equation 23 into Equation 19, we get:

$$\frac{\partial g}{\partial \tau} = \frac{\partial^2 g}{\partial X^2} + \frac{d^2 w}{dX^2} \quad [26]$$

It can be separated as the following two equations.

$$\frac{\partial g}{\partial \tau} = \frac{\partial^2 g}{\partial X^2} \quad [27]$$

$$\frac{d^2 w}{dX^2} = 0 \quad [28]$$

We can first solve $\frac{d^2 w}{dX^2} = 0$ with the boundary conditions listed in Equation 25 and obtain:

$$w(X) = -\frac{\delta}{2} X + B \quad [29]$$

where B is an arbitrary constant for integration, which cannot be found using the flux boundary conditions for $w(X)$.

So far, the solution is:

$$C(X, \tau) = g(X, \tau) + w(X) = g(X, \tau) - \frac{\delta}{2} X + B \quad [30]$$

The next step is to solve for $g(X, \tau)$ by the SOV approach, assuming $g(X, \tau) = \theta(X)T(\tau)$, where $\theta(X)$ is a function of X and $T(\tau)$ is a function of τ alone.

$$g(X, \tau) = \sum_{n=1}^{\infty} A_n \cos(n\pi X) \exp(-n^2 \pi^2 \tau) \quad [31]$$

The solution is mostly complete from Equations 30 and 31, except for the constant B .

$$C(X, \tau) = \sum_{n=1}^{\infty} A_n \cos(n\pi X) \exp(-n^2 \pi^2 \tau) - \frac{\delta}{2} X + B \quad [32]$$

Now, we can use the initial condition in Equation 20 to solve for the constants B and A_n . When $\tau = 0$, the Equation 32 becomes:

$$\sum_{n=1}^{\infty} A_n \cos(n\pi X) - \frac{\delta}{2} X + B = 1 \quad [33]$$

According to the Sturm-Liouville theory, we can obtain the solution of A_n from Equation 34, where IC is the initial condition, ω_n represents the eigenfunction, and $r(X)$ represents the weighting function. In this example, $\omega_n = \cos(n\pi X)$ and $r(X) = 1$.

$$A_n = \frac{\int_0^1 (IC - w(X)) \omega_n r(X) dX}{\int_0^1 \omega_n^2 r(X) dX} \quad [34]$$

Therefore:

$$A_n = \frac{\int_0^1 (IC - w(X)) \omega_n r(X) dX}{\int_0^1 \omega_n^2 r(X) dX} = \frac{\delta(-1 + \cos(n\pi))}{n^2 \pi^2} \quad [35]$$

For even n , $\cos(n\pi) = 1$, and A_n vanishes. Thus, the infinite series of Equation 31 only consists of odd-numbered terms.

To get the constant B , we can multiply the weighting function $r(X)$ on both sides in Equation 33 and integrate over X from 0 to 1.

$$\sum_{n=1}^{\infty} A_n \int_0^1 \cos(n\pi X) dX - \int_0^1 \frac{\delta}{2} X dX + \int_0^1 B dX = \int_0^1 1 dX \quad [36]$$

Since the first term $\sum_{n=1}^{\infty} A_n \int_0^1 \cos(n\pi X) dX$ goes to zero, we get:

$$B = 1 + \frac{\delta}{4} \quad [37]$$

Hence, the full analytical solution of the dimensionless concentration profile is:

$$C(X, \tau) = \left[\sum_{n=1}^{\infty} \frac{\delta(-1 + \cos(n\pi))}{n^2 \pi^2} \cos(n\pi X) \exp(-n^2 \pi^2 \tau) \right] - \frac{\delta}{2} X + 1 + \frac{\delta}{4} \quad [38]$$

The steady-state concentration profile is:

$$C(X, \infty) = -\frac{\delta}{2} X + 1 + \frac{\delta}{4} \quad [39]$$

The infinite series in Equation 38 can be reasonably approximated by its first $n = 5$ terms except for short times. Of note, for cycling simulations, the coefficients A_n need to be updated for each change in the galvanostatic boundary conditions, corresponding to the reversal of polarity, but the steady-state term remains unchanged. In simulating cell cycling, since the values of the coefficients A_n are arrived at using the initial concentration profile in Equation 34, the concentration profile at the end of a given cycle must be used as the initial profile for the succeeding one. In other words, the coefficients for two successive cycles are mathematically related and establish the relationship between the concentration profiles.²⁷

It is also worth noting that the electrostatic potential profile given in Equation 15 has to be solved numerically due to the presence of the infinite series in $C(X, \tau)$ and the nonlinearity of the potential equation. A Gaussian quadrature numerical integration can be applied to get the terminal potential at $x = 0$. This method is illustrated in the Appendix. Alternatively, $C(X, \tau)$ can be solved numerically using Finite Volume Methods (FVM).

Finite volume formulation of EN-NP.—FVM discretizes the computational domain into finite volumes, and explicitly considers the fluxes of each variable through each finite volume. Since this involves the summation of the fluxes entering and leaving each volume, the FVM scheme is conservative, which is a major advantage. It is also easier to extend to unstructured grids compared to standard Finite Difference Methods (FDM).

The computational domain can be divided into n elements, each of size h (n thus denotes the number of internal nodes). To apply the finite volume method, a (discrete) flux balance for each control volume need to be elucidated. We integrate Equation 1 from $(j-1)h$ to jh , giving us the dimensionless FVM formulation as:

$$\frac{dC_{j-1/2}}{d\tau} = -\frac{N_j - N_{j-1}}{h} \quad [40]$$

where the subscript j represents the spatially discretized variable index and varies from 1 to $n + 1$.

The first-order approximation can be applied for the flux:

$$N_j = -\frac{C_{j+1/2} - C_{j-1/2}}{h} \quad [41]$$

Figure 2 shows a schematic drawing of a cell-centered three-element (two internal nodes) FVM scheme and ghost points. Previous applications of FVM methods for lithium-ion batteries have been reported elsewhere.²⁹ FVM approach with n elements provides the discretized

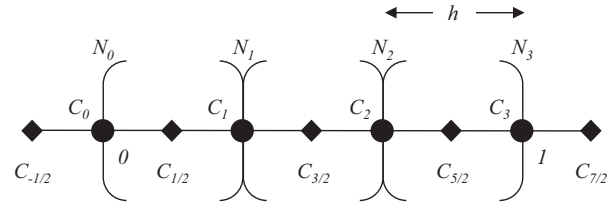


Figure 2. A two-internal-node (three-element) FVM scheme.

equations for the original PDE as given below.

$$\frac{dC_{1/2}}{d\tau} = -\frac{\left(-\frac{C_{3/2}-C_{1/2}}{h}\right) - \left(\frac{\delta}{2}\right)}{h} \quad [42]$$

$$\frac{dC_{j-1/2}}{d\tau} = -\frac{\left(-\frac{C_{j+1/2}-C_{j-1/2}}{h}\right) - \left(-\frac{C_{j-1/2}-C_{j-3/2}}{h}\right)}{h}, j = 2 \dots n \quad [43]$$

$$\frac{dC_{n+1/2}}{d\tau} = -\frac{\left(\frac{\delta}{2}\right) - \left(-\frac{C_{n+1/2}-C_{n-1/2}}{h}\right)}{h} \quad [44]$$

A simple averaging procedure is used to approximate the concentrations at the boundaries ($X = 0$ and $X = 1$ respectively) as:

$$C_0 = \frac{C_{1/2} + C_{-1/2}}{2} \text{ and } C_3 = \frac{C_{5/2} + C_{7/2}}{2} \quad [45]$$

Higher order approximations can also be used to find the values at the boundaries.

Poisson-Nernst-Planck Model.—The Poisson-Nernst-Planck equations represent a mean-field continuum approximation of the dynamics of ionized electrolyte under the influence of the electrostatic field in a dilute system. The PNP model is restricted to the dilute solution regime. The electrolyte acts as a conducting liquid, and the ions create a continuous concentration profile across the system. The PNP model provides quantitative predictions, and it is useful for relating system-level experimental data to the local electrochemistry.

Poisson's equation relates the charge density and the Laplacian of the electric potential (ϕ). For the binary electrolyte considered for lithium symmetric cells, it is represented in 1-D as:

$$\frac{\partial^2 \phi}{\partial x^2} = -\frac{F}{\epsilon_0 \epsilon_s} (z_1 c_1 + z_2 c_2) \quad [46]$$

where the boundary conditions for ϕ are listed in Table II.

The explicit specification of the potential distribution now necessitates additional boundary conditions for ϕ . For simplicity, the “zero-field” condition of Streeter and Compton^{12,18} is used at the electrode, $x = 0$. A reference value for electrostatic potential is taken at $x = L$.

The full PNP system is comprised of 7, 8, 46, and the boundary conditions listed in Table I and Table II. When $t = 0$, the bulk concentrations of both ions are such that $c_1 = c_2 = c_0$.

For computational convenience and analysis, the PNP equations can be scaled and transformed by the following dimensionless variables and scale factors:

$$C_i = \frac{c_i}{c_0}, X = \frac{x}{L}, \Phi = \frac{z_1 F}{RT} \phi, \text{ and } \tau = \frac{D_1}{L^2} t \quad [47]$$

$$\varepsilon = \sqrt{\frac{RT \epsilon_s \epsilon_0}{z_1^2 F^2 c_0 L^2}}, \delta = \frac{I_{app} L}{z_1 F c_0 D_1}, \text{ and } \xi = \frac{D_2}{D_1} \quad [48]$$

Table II. Boundary conditions for Poisson's equation.

$x = 0$	$x = L$
$\frac{\partial \phi}{\partial x} = 0$	$\phi = 0$

Table III. Dimensionless PNP system ($z_1 = 1$, $z_2 = -1$).

i	Governing Equations	$X = 0$	$X = 1$
1	$\frac{\partial C_1}{\partial \tau} = \frac{\partial^2 C_1}{\partial X^2} + C_1 \frac{\partial^2 \Phi}{\partial X^2} + \frac{\partial C_1}{\partial X} \frac{\partial \Phi}{\partial X}$	$-\frac{\partial C_1}{\partial X} _{X=0} - C_1 \frac{\partial \Phi}{\partial X} _{X=0} = \delta$	$-\frac{\partial C_1}{\partial X} _{X=1} - C_1 \frac{\partial \Phi}{\partial X} _{X=1} = \delta$
2	$\frac{\partial C_2}{\partial \tau} = \xi \left(\frac{\partial^2 C_2}{\partial X^2} - C_2 \frac{\partial^2 \Phi}{\partial X^2} - \frac{\partial C_2}{\partial X} \frac{\partial \Phi}{\partial X} \right)$ $\frac{\partial^2 \Phi}{\partial X^2} = -\frac{1}{\epsilon^2} (C_1 - C_2)$	$-\frac{\partial C_2}{\partial X} _{X=0} + C_2 \frac{\partial \Phi}{\partial X} _{X=0} = 0$ $\frac{\partial \Phi}{\partial X} _{X=0} = 0$	$-\frac{\partial C_2}{\partial X} _{X=1} + C_2 \frac{\partial \Phi}{\partial X} _{X=1} = 0$ $\Phi _{X=1} = 0$

The dimensionless PNP system and the boundary conditions are listed in Table III.

For the symmetric cell, we assume zero anion flux at each electrode, implying that the average concentration of the PF_6^- ions in the cell remains unchanged with time. In addition, since we have the same current density at both electrodes, the rate of stripping and deposition of lithium at the electrodes is equal. Therefore, the average Li^+ concentration in the cell is equal to its initial value, and we can integrate microscopic PDEs, Equations 1 and 2, spatially from 0 to L and get:

$$\begin{aligned} \frac{\partial \int_0^L c_1 dx}{\partial t} &= L \frac{\partial c_{1,avg}}{\partial t} = -(N_1|_{x=L} - N_1|_{x=0}) \\ &= -\left(\frac{I_{app}}{z_1 F} - \frac{I_{app}}{z_1 F} \right) = 0 \end{aligned} \quad [49]$$

$$\begin{aligned} \frac{\partial \int_0^L c_2 dx}{\partial t} &= L \frac{\partial c_{2,avg}}{\partial t} = -(N_2|_{x=L} - N_2|_{x=0}) = -(0 - 0) = 0 \end{aligned} \quad [50]$$

Thus, after applying the dimensionless groups (Equation 47) and integrating the Equations 49 and 50 in time with the initial condition, we can get:

$$C_{1,avg} = \int_0^1 C_1 dX = 1 \text{ and } C_{2,avg} = \int_0^1 C_2 dX = 1 \quad [51]$$

Microscopic PDEs and macroscopic balances (Equations 49 and 50) are thus always related, and the reduction is obvious for Neumann boundary conditions.

With this knowledge of average ion concentrations, we can integrate the Poisson's equation in X from 0 to 1 and obtain:

$$\left. \frac{\partial \Phi}{\partial X} \right|_{X=1} - \left. \frac{\partial \Phi}{\partial X} \right|_{X=0} = -\frac{1}{\epsilon^2} (C_{1,avg} - C_{2,avg}) = 0 \quad [52]$$

Therefore, when the potential gradient at one end is defined, its value at the other boundary is automatically determined from Equation 52. In our analysis, the zero-field assumption at $X = 0$ leads to the same condition at $X = 1$. This is exactly satisfied for conservative discretization schemes. For non-conservative convergent numerical schemes, it might result in a finite but small non-zero value, which approaches zero as the computational grid is refined.

Finite Volume formulation of PNP.—Similar to EN-NP model, FVM scheme is used for the PNP model. It inherits the advantages in

simplicity as shown in the EN-NP model. The domain can be divided into n elements (n denotes the number of internal nodes) with constant grid spacing h . To apply the FVM, we integrate Equations 1 and 2 over a single volume element, from $(j-1)h$ to jh , giving us the FVM formulation for species 1 and 2 as:

$$\frac{dC_{1,j-1/2}}{d\tau} = -\left(\frac{N_{1,j} - N_{1,j-1}}{h} \right) \quad [53]$$

$$\frac{dC_{2,j-1/2}}{d\tau} = -\left(\frac{N_{2,j} - N_{2,j-1}}{h} \right) \quad [54]$$

where j represents the spatial discretization and j is from 1 to n .

The first-order approximation can be applied for the flux:

$$\begin{aligned} N_{1,j} &= -\frac{\partial C_1}{\partial X} - C_1 \frac{\partial \Phi}{\partial X} = -\frac{C_{1,j+1/2} - C_{1,j-1/2}}{h} \\ &\quad - C_{1,j} \frac{\Phi_{j+1/2} - \Phi_{j-1/2}}{h} \end{aligned} \quad [55]$$

$$\begin{aligned} N_{2,j} &= -\frac{\partial C_2}{\partial X} + C_2 \frac{\partial \Phi}{\partial X} = -\frac{C_{2,j+1/2} - C_{2,j-1/2}}{h} \\ &\quad + C_{2,j} \frac{\Phi_{j+1/2} - \Phi_{j-1/2}}{h} \end{aligned} \quad [56]$$

In contrast to the simpler flux expression in EN-NP (Equation 41), the PNP flux discretization requires concentration at the ends of each element (Equations 55 and 56). If the concentration is defined at the midpoint of the element, the face concentrations ($C_{1,j}$, $C_{2,j}$) are also needed. A strict FVM solves concentration as a piecewise continuous function, and the value $C_{i,j}$ is not known. The flux is calculated based on the local velocity. In this paper, we assume that $C_{1,j}$ is the average of $C_{1,j-1/2}$ and $C_{1,j+1/2}$ as Equation 57.

$$C_{1,j} = \frac{C_{1,j-1/2} + C_{1,j+1/2}}{2} \quad [57]$$

This will introduce errors and oscillations in strongly convective PDEs, but this approximation appears to work for the PNP case. In order to avoid approximating the $C_{i,j}$, a piecewise linear profile can be assumed to arrive at a control-volume scheme as demonstrated earlier by Zeng et al.³⁰ However, this will result in a tri-diagonal mass matrix for the accumulation terms.

The FVM form of the Equations 53 and 54 become

$$\frac{dC_{1,1/2}}{d\tau} = -\left(\frac{-\frac{C_{1,3/2} - C_{1,1/2}}{h} - C_{1,1} \frac{\Phi_{3/2} - \Phi_{1/2}}{h}}{h} \right) - \delta \quad [58]$$

$$\frac{dC_{1,j-1/2}}{d\tau} = -\left(\frac{-\frac{C_{1,j+1/2} - C_{1,j-1/2}}{h} - C_{1,j} \frac{\Phi_{j+1/2} - \Phi_{j-1/2}}{h}}{h} \right) - \left(\frac{-\frac{C_{1,j-1/2} - C_{1,j-3/2}}{h} - C_{1,j-1} \frac{\Phi_{j-1/2} - \Phi_{j-3/2}}{h}}{h} \right), j = 2 \dots n \quad [59]$$

$$\frac{dC_{1,n+1/2}}{d\tau} = -\left(\frac{\delta - \left(\frac{C_{1,n+1/2} - C_{1,n-1/2}}{h} - C_{1,n} \frac{\Phi_{n+1/2} - \Phi_{n-1/2}}{h} \right)}{h} \right) \quad [60]$$

Similarly, the dimensionless concentration expressions for species 2 are:

$$\frac{dC_{2,1/2}}{d\tau} = -\xi \frac{\left(-\frac{C_{2,3/2}-C_{2,1/2}}{h} + C_{2,1} \frac{\Phi_{3/2}-\Phi_{1/2}}{h}\right) - 0}{h} \quad [61]$$

$$\frac{dC_{2,j-1/2}}{d\tau} = -\xi \frac{\left(-\frac{C_{2,j+1/2}-C_{2,j-1/2}}{h} + C_{2,j} \frac{\Phi_{j+1/2}-\Phi_{j-1/2}}{h}\right) - \left(-\frac{C_{2,j-1/2}-C_{2,j-3/2}}{h} + C_{2,j-1} \frac{\Phi_{j-1/2}-\Phi_{j-3/2}}{h}\right)}{h}, j = 2 \dots n \quad [62]$$

$$\frac{dC_{2,n+1/2}}{d\tau} = -\xi \frac{0 - \left(-\frac{C_{2,n+1/2}-C_{2,n-1/2}}{h} + C_{2,n} \frac{\Phi_{n+1/2}-\Phi_{n-1/2}}{h}\right)}{h} \quad [63]$$

Also, the FVM discretization for dimensionless electrostatic potential can be expressed as:

$$-\frac{\left(-\frac{\Phi_{3/2}-\Phi_{1/2}}{h}\right) - 0}{h} = -\frac{1}{\varepsilon^2} (C_{1,1/2} - C_{2,1/2}) \quad [64]$$

$$-\frac{\left(-\frac{\Phi_{j+1/2}-\Phi_{j-1/2}}{h}\right) - \left(-\frac{\Phi_{j-1/2}-\Phi_{j-3/2}}{h}\right)}{h} = -\frac{1}{\varepsilon^2} (C_{1,j-1/2} - C_{2,j-1/2}), j = 2 \dots n \quad [65]$$

$$-\frac{\left(-\frac{2\Phi_{n+1/2}}{h}\right) - \left(-\frac{\Phi_{n+1/2}-\Phi_{n-1/2}}{h}\right)}{h} = -\frac{1}{\varepsilon^2} (C_{1,n+1/2} - C_{2,n+1/2}) \quad [66]$$

The PNP DAE system has the initial conditions given by

$$C_{1,j-1/2} = 1, j = 1 \dots n + 1 \quad [67]$$

$$C_{2,j-1/2} = 1, j = 1 \dots n + 1 \quad [68]$$

$$\Phi_{j-1/2} = 0, j = 1 \dots n + 1 \quad [69]$$

We can obtain equations at $x = 0$ as:

$$C_{1,0} = \frac{C_{1,1/2} + C_{1,-1/2}}{2} = C_{1,1/2} + \frac{\delta}{2}h \quad [70]$$

$$C_{2,0} = \frac{C_{2,1/2} + C_{2,-1/2}}{2} = C_{2,1/2} \quad [71]$$

$$\Phi_0 = \frac{\Phi_{1/2} + \Phi_{-1/2}}{2} = \Phi_{1/2} \quad [72]$$

Higher order approximations can be used to find the values at $X = 0$ and 1, but the observed order of convergence remains the same for the PNP model.

In previous work from our group, we had performed reformulation to increase the computational efficiency which primarily has relevance for estimation and real-time control for Battery Management Systems. In this paper, reformulation was not performed. Some possible directions for computationally efficient methods for PNP-type models are outlined below. These will be pursued in future work.

- (1) For a FVM or FDM formulations, the equation for the potential is linear and the values for the potential at different node points (or elements can) be written in terms of the species concentrations C_1 and C_2 . This involves finding the eigenvalues and eigenvectors for any number of node points/elements, N .³¹
- (2) As opposed to FVM, Galerkin or orthogonal collocation approach results in faster convergence. The best possible approach for applying spectral methods for PNP was presented earlier.³²⁻³⁴
- (3) Both 1 and 2 assume the use of adaptive integrators in time. It is possible to arrive at higher order methods in both space and time using the model equations.
- (4) For this particular model, steep gradients are confined to the thin double layers in the vicinity of the electrodes. We can thus solve the model as a 3-region problem, (i.e., as three domains given

by $[0,\delta]$, $[\delta,1-\delta]$, and $[1-\delta,1]$ where δ is of order of the double layer thickness. This will help achieve greater efficiency through optimal resolution of the bulk and boundary regions, even though the three PDEs are solved individually in the three regions.^{32,35}

Results and Discussion

Analytical and numerical solutions of EN-NP.—In this study, we chose the parameters listed in Table IV, which are a reasonable representation of experimental conditions. Some of the values may be found in Wood et al.⁹

We used separation of variables techniques to find the analytical form of solutions in concentration, and the analytical solution of the dimensionless concentration profile as Equation 38. The spatial concentration profiles at a given instant can be obtained by substituting dimensionless time into the equation.

We solved the discretized equations in time using IDA, an Implicit Differential-Algebraic solver in ANSI-standard C language under BSD license. Developed by Hindmarsh et al. IDA is an efficient solver for initial value problems (IVP) for systems of DAEs, which is part of the SUNDIALS (SUite of Nonlinear and Differential/ALgebraic equation Solvers) package.³⁶ We chose an absolute solver tolerance of 1×10^{-8} and relative tolerance of 1×10^{-7} , which we expect to be sufficiently stringent accuracy conditions for relevant situations in experiments and control. In addition, we limited the maximum order of the BDF (Backward Differentiation Formulae) to 2 to ensure numerical 'A-stability'.³⁷ We simulated the model for an hour and demonstrated the transitions in concentration and potential profiles. Since the electrodes are the location of the greatest variation of electrochemical variables, and we are interested in their influence on electrode kinetics, the values of the concentration and potential are examined at $X = 0$. The number of internal nodes was chosen to ensure accuracy up to 6 decimal places.

Table IV. Base case simulation parameters.

Symbol	Physical meaning	Value	Units
c_0	Initial concentration of the electrolyte	500	mol/m ³
D_1	Diffusivity of Li ⁺	4×10^{-10}	m ² /s
D_2	Diffusivity of PF ₆ ⁻	4×10^{-9}	m ² /s
I_{app}	Applied current density	10.0	A/m ²
L	Cell dimension in x	7.5×10^{-4}	m
T	Temperature	298.15	K
ε_0	Vacuum permittivity	8.85×10^{-12}	kg ⁻¹ m ⁻³ s ⁴ A ²
ε_s	Dielectric constant of the solvent	16.8	-

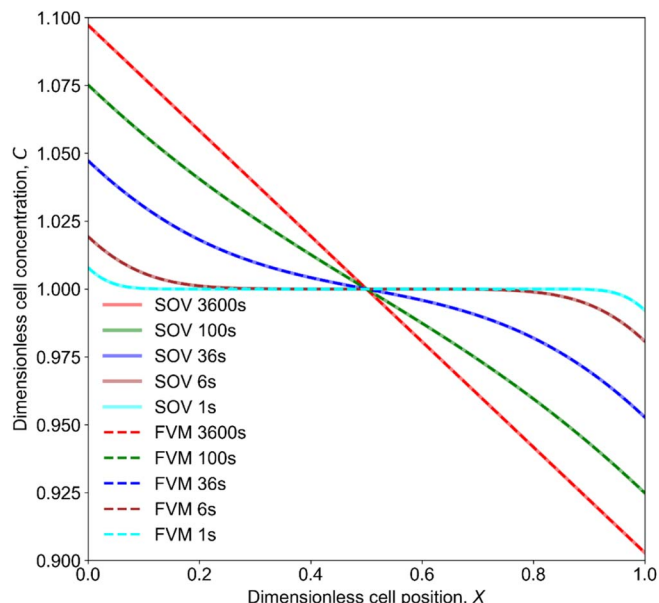


Figure 3. Solutions of the EN-NP system for spatial concentration profiles.

After substitution of the boundary conditions into the internal governing equations, the EN-NP model yields an initial value problem for a system of ODEs (DAEs if we solve for ϕ as well). The numerical solutions exhibit agreement with the analytical solutions as in Figure 3 and Figure 4. At short times, we observe a boundary layer near the electrodes in the concentration and potential profiles, while for longer times, the variables attain the linear profile described by the steady-state solution of Equation 39. Hence, at longer times, convergence is achieved with relatively fewer node points.

Table V reports the simulated dimensionless concentration solution by FVM scheme at $x = 0$ and $t = 1$ s. The convergence rate of the method was evaluated by using the data listed in Table V and comparing it with the analytical solution. To facilitate the convergence analysis, grid spacing values ranging from $h = 1/4$ to $h = 1/512$ (eight values) were used. We avoided using grid sizes below $h = 1/2048$ to prevent errors from the saturation of numerical accuracy due to the

Table V. The EN-NP solutions for C_0 when $t = 1$ s by FVM scheme
Analytical solution: $C_0 = 1.00788467719606$.

Spacing (h)	FVM
1/4	1.02528612650271
1/8	1.01407707486321
1/16	1.00954921773040
1/32	1.00826831827022
1/64	1.00797894991306
1/128	1.00790870306024
1/256	1.00789114377750
1/512	1.00788687365799
1/1024	1.00788569105244
1/2048	1.00788557426487

tolerance settings. In obtaining convergence rate estimates, we used least-squares regression to find the slope of the logarithm of the absolute error (the difference between numerical and analytical solutions) versus $\log(h)$. For FVM, the slope is 1.911269, respectively, indicating nearly second order convergence even at short times.

Comparison of EN-NP and PNP results.—Table VI reports the difference of the values between EN-NP (analytical solutions) and PNP using 2000 internal nodes, at $x = 0$. We observed that the solutions of EN-NP at $x = 0$ were roughly the average of C_1 and C_2 . From Figure 5, and Figure 6, it is reasonable to use EN-NP to replace the PNP to achieve efficient simulation because the differences of concentration and potential at $x = 0$ up to an hour are mostly negligible for practical applications. While a scaling analysis based on model parameters can determine the applicability of EN-NP a priori, a goal of this paper is to provide a robust code with the ability to simulate the PNP model for a wide range of parameter combinations and regimes where the departure from electroneutrality may become significant.

The convergence analysis is repeated to examine the solution $x = 0$ when $t = 1$ s. The numerical results are shown in Table VII. We used the results with $h = 1/2048$ as the benchmark to conduct the analysis. Taking spacing from $1/16$ to $1/1024$, the slope for C_1 , C_2 , and the potential are 1.189440, 1.074816 and 1.091390, respectively. Thus, only first order convergence is found for PNP, as opposed to the second order obtained for the EN-NP model. A detailed examination of the utility of a numerical scheme and its convergence characteristics for the PNP model is beyond the scope of this paper. However, while the use of the PNP model may be tempting for physical detail, the faster convergence of the EN-NP model may result in accurate and meaningful solutions with a substantially smaller number of node points or elements.

Effect of ϵ .—Table VIII reports solutions of the PNP model at relatively short times (1 s), as a function of the parameter ϵ . ϵ is a measure of the ratio of double-layer thickness to the characteristic system size, and it is useful to examine its effect on the solution. The results indicate a negligible change ($\sim 0.5\%$) in the dimensionless solutions below a certain lower threshold of ϵ . From a simulations standpoint, this means that for systems with ϵ values below this threshold, the solution obtained using the threshold ϵ may be used as an adequate approximation of that with the actual parameter set. This is because

Table VI. The deviation between EN-NP and PNP solutions.

Time (s)	$ C_{1,0}^{PNP} - C_{1,0}^{EN-NP} $	$ C_{2,0}^{PNP} - C_{2,0}^{EN-NP} $	$ \phi_0^{PNP} - \phi_0^{EN-NP} $ (V)
3600	4.855842×10^{-5}	4.855843×10^{-5}	3.544208×10^{-6}
100	4.982804×10^{-5}	4.728882×10^{-5}	2.449541×10^{-6}
36	4.933402×10^{-5}	4.778283×10^{-5}	2.480222×10^{-6}
6	4.956565×10^{-5}	4.755120×10^{-5}	2.439985×10^{-6}
1	4.946024×10^{-5}	4.765661×10^{-5}	2.437030×10^{-6}

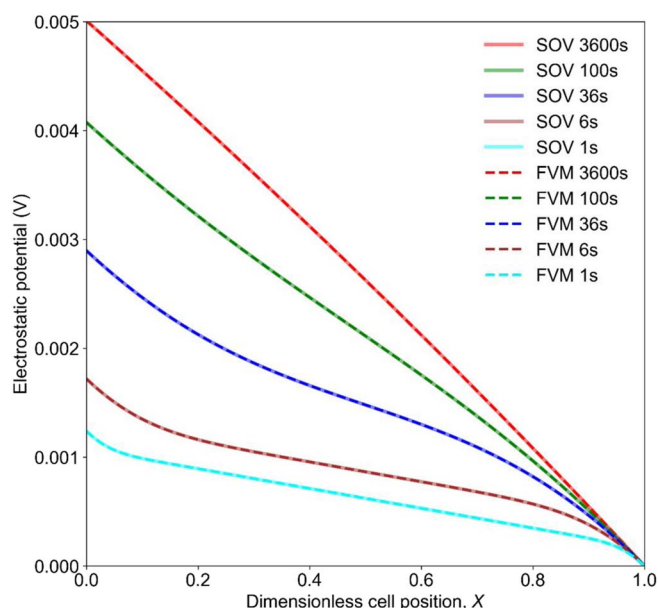


Figure 4. Solutions of EN-NP system for electrostatic potential.

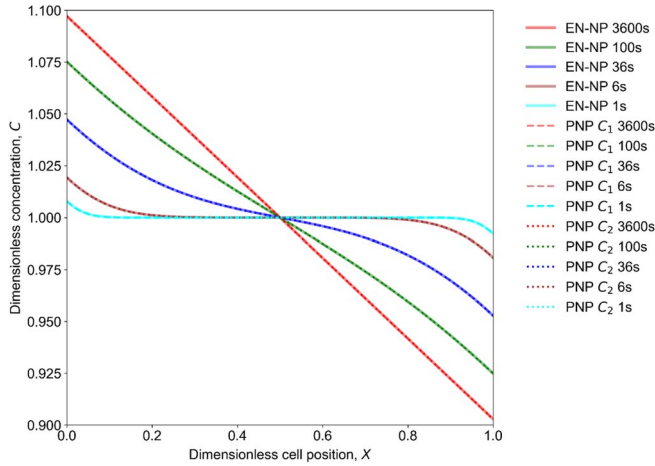


Figure 5. Comparison of the concentration profiles obtained from the different methods illustrating the expected agreement between both models.

it is easier to treat larger values of ε numerically. The concept is similar to perturbation methods. It must be noted that even though the dimensionless solutions are nearly equal, the corresponding solutions obtained after transformation back to dimensional variables may differ in value depending on the specific set of parameters used. In addition, the specific value of this threshold is likely to vary with the design and transport parameters.

Case Study: Comparing the Model with Experimental Li||Cu In Situ Cell Data:

To illustrate the application of the above computational models to inform our understanding of cell voltage response dynamics, we compared model predictions against experimental data. The experimental voltage response data was generated from a Lithium-Copper (Li-Cu) electrochemical cell. The detailed description and experimental set-up may be found in the Appendix. We used the conservative FVM model for transport, along with an electrode kinetics model to calculate the cell-voltage response. Figure 7 depicts representative voltage-time data. In Phase 1, Li is stripped from the bulk Li electrode and

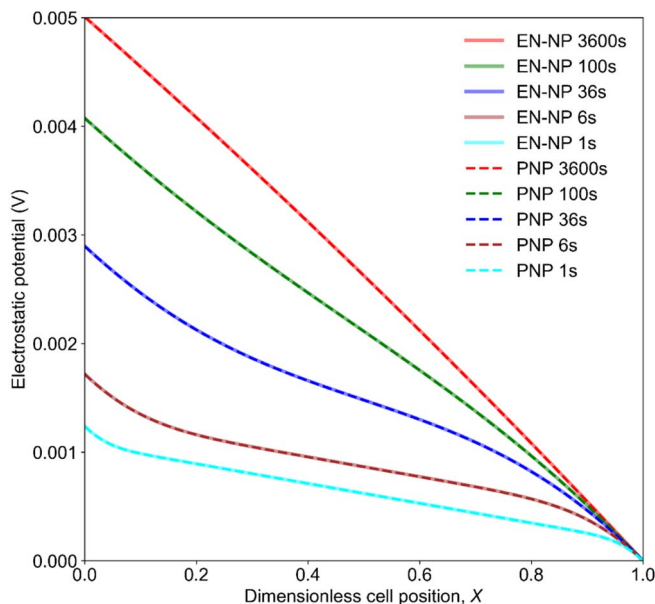


Figure 6. Comparison of PNP and EN-NP model in electrostatic potential.

Table VII. The PNP solutions at $x = 0$ when $t = 1$ s by FVM scheme.

h	C_1 (dimensionless)	C_2 (dimensionless)	ϕ (V)
1/4	1.049577	1.000995	0.720212×10^{-3}
1/8	1.026223	1.001931	0.876889×10^{-3}
1/16	1.015622	1.003477	0.996921×10^{-3}
1/32	1.011305	1.005232	0.109930×10^{-2}
1/64	1.009497	1.006461	0.116515×10^{-2}
1/128	1.008668	1.007150	0.120131×10^{-2}
1/256	1.008271	1.007512	0.122018×10^{-2}
1/512	1.008077	1.007697	0.122974×10^{-2}
1/1024	1.007981	1.007791	0.123452×10^{-2}
1/2048	1.007933	1.007838	0.123692×10^{-2}

deposited on the initially bare Cu substrate. In Phase 2, Li is stripped back from the Cu side (active Li is limited) and deposited at the Li end. The direction of the applied current density is reversed in Phase 3, and the stripping and deposition switch back to the Li and Cu ends respectively. After Phase 1, sufficient Li is regarded to have deposited on Cu to approximate a Li||Li cell. In particular, a drop in voltage may be observed in Phase 3, which may be a signature of transitions in electrodeposition and electro-dissolution pathways, as determined by Wood et al. via operando studies.⁹

In Wood et al., the transition between deposition and dissolution mechanisms is considered via a lumped, parallel pathway mechanism. Each reaction pathway is modeled as an electrode reaction described by a Butler-Volmer (BV)-type expression. The kinetic model equation at both stripping and deposition electrodes is given by:³⁸

$$i = i_{0,ref} \left(\frac{c_{Li^+}(x,t)}{c_{ref}} \right)^{\alpha_a} \left\{ \exp \left(\frac{\alpha_a F \eta(t)}{RT} \right) - \exp \left(-\frac{\alpha_c F \eta(t)}{RT} \right) \right\} \quad [73]$$

Here, $i_{0,ref}$ is an ‘effective’ exchange current density that includes the contributions of the ‘fast’ and ‘slow’ reactions. α_a and α_c are anodic and cathodic charge transfer coefficients, and the other symbols have their usual meaning. The lithium ion concentration at the electrode is denoted by $c_{Li^+}(x,t)$. $i_{0,ref}$ may be written as $i_{0,ref} = \theta i_{0,fast} + (1 - \theta) i_{0,slow}$, where $i_{0,fast}$ and $i_{0,slow}$ are reference exchange current densities proportional to the rate constants of the slow and fast reactions respectively. These parameters are lumped quantities that encode differences in deposit morphology, surface reactivity, inhomogeneities in the Solid Electrolyte Interphase (SEI), local ion transport effects and other complexities. The quantity θ denotes the surface coverage of the kinetically fast deposits.

The electrode potentials $\phi_s(t)$ are determined using the relation

$$\eta(t) = \phi_s(t) - \phi(t) \quad [74]$$

assuming zero open-circuit potential for the Li-metal reaction $Li^+ + e^- \rightleftharpoons Li$.

The cell voltage is thus defined as the difference between the computed $\phi_s(t)$ at each electrode:

$$V_{cell} = \phi_s^c - \phi_s^a \quad [75]$$

Table VIII. PNP solutions at $X = 0$ and $t = 1$ s for different values of ε . The base case value: $\varepsilon_0 = 3.76 \times 10^{-7}$; $\delta = 0.38$.

ε	C_1 (dimensionless)	C_2 (dimensionless)	ϕ (V)
ε_0	1.008885	1.006961	1.191527×10^{-3}
$\varepsilon_0 \times 10$	1.008885	1.006961	1.191479×10^{-3}
$\varepsilon_0 \times 10^2$	1.008885	1.006961	1.191470×10^{-3}
$\varepsilon_0 \times 10^3$	1.008886	1.006960	1.191401×10^{-3}
$\varepsilon_0 \times 10^4$	1.008986	1.006839	1.184991×10^{-3}
$\varepsilon_0 \times 10^5$	1.010807	1.003693	1.001104×10^{-3}
$\varepsilon_0 \times 10^6$	1.011778	1.000093	4.713492×10^{-5}

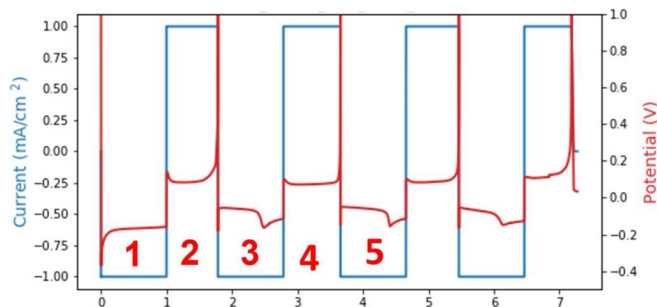


Figure 7. Experimental current and voltage profiles for the Li-Cu electrochemical cell at an applied current density of 1 mA/cm².

The calculation of the surface area fractions θ as a function of time, and thus $i_{0,ref}$ necessitates assumptions about the morphology of the electrodeposits.^{9,16} In this study, we circumvented the need for assumptions by attempting the direct fitting of $i_{0,ref}$ at each electrode as a function of time. Thus:

$$i = i_{0,ref}(t) \left(\frac{c_{Li^+}(x, t)}{c_{ref}} \right)^{\alpha_a} \left\{ \left[\exp \left(\frac{\alpha_a F \eta(t)}{RT} \right) - \exp \left(-\frac{\alpha_c F \eta(t)}{RT} \right) \right] \right\} \quad [76]$$

The parameterization problem is thus the determination of $i_{0,ref}(t)$ profiles that minimize the error between the simulated and experimental values of the voltage response. We refer to these by $i_{0,effa}$ and $i_{0,effc}$ for the stripping and deposition electrodes respectively. In this example, the Mean Absolute Error (MAE) between model and experiment is used as the objective function, which is minimized. In addition, we focus solely on the Phases 3 and 5 in Figure 7 in an attempt to capture the sharp voltage transition therein, and verify our predictions against data and literature reports.

In the systems approach, the effective exchange current density at each electrode was assumed as a piecewise quadratic profile in

Lagrange form with two stages. Mathematically this is illustrated as:

$$i_{0,ref}(t) = \begin{cases} i_1 \frac{t-t_1}{0-t_1} \cdot \frac{t-2t_1}{0-2t_1} + i_2 \frac{t-0}{t_1-0} \cdot \frac{t-2t_1}{t_1-2t_1} + i_3 \frac{t-0}{2t_1-0} \cdot \frac{t-t_1}{2t_1-t_1} & 0 \leq t \leq 2t_1 \\ i_3 \frac{T-t_2}{0-t_2} \cdot \frac{T-2t_2}{0-2t_2} + i_4 \frac{T-0}{t_2-0} \cdot \frac{T-2t_2}{t_2-2t_2} + i_5 \frac{T-0}{2t_2-0} \cdot \frac{T-t_2}{2t_2-t_2} & 2t_1 \leq t \leq 2t_1 + 2t_2 \end{cases} \quad [77]$$

$$t_1 = \frac{2500-0}{2}, \quad t_2 = \frac{3600-2500}{2}, \quad T = t - 2t_1$$

This mathematical form was assumed for both $i_{0,effc}$ and $i_{0,effa}$. The experimental data was divided into two sets, before and after the voltage transition ($t \sim 2500$ s). This results in 5 parameters ($i_1 - i_5$) for $i_{0,ref}(t)$ at each electrode. The experimental data were sampled every 5 seconds over the whole half-cycle, and the upper and lower bound for exchange current densities were set at 0.1 and 100 A/m² respectively. The Global Optimization package in *Maple 2018* was used which uses a differential evolution approach for optimization. Results were also verified using gradient-based algorithms.

Figure 8 illustrates the agreement between the simulated voltage response and experimental data, even with this simplified model of exchange current density variation. The use of quadratic polynomials provided better fits compared to a piecewise linear approximation for the current density, but higher order polynomials provided only marginal reduction in error. In this case, the MAE corresponding to the optimal values of the coefficients i_j of Equation 77 is approximately 5 mV.

Figure 9 shows the variation of overpotentials as a function of time. It can be seen that the fitted polynomials predict a sharp drop in overpotential at the Cu electrode, in addition to a smaller increase at the Li electrode. The anodic signature is likely due to the transition between ‘fast’ and ‘slow’ pathways. At the Li electrode, this may be the exhaustion of electrochemically deposited Li and their associated faster kinetics, and the gradual transition to stripping from the bulk. The sharp drop at the Cu electrode is more pronounced and suggests a transition in which Li deposits via the formation of new nuclei as opposed to growing on existing deposits, possibly due to passivation by SEI formation. This likely explains the sudden drop followed by a gradual rise in overpotential. The fitted profiles were verified by simulation and comparison with multiple data sets and exhibited adequate agreement for each case. The trends in electrode polarization track the variations in fitted reference exchange current density of Figure 10. The increase in polarization of both electrodes is due to the reduction

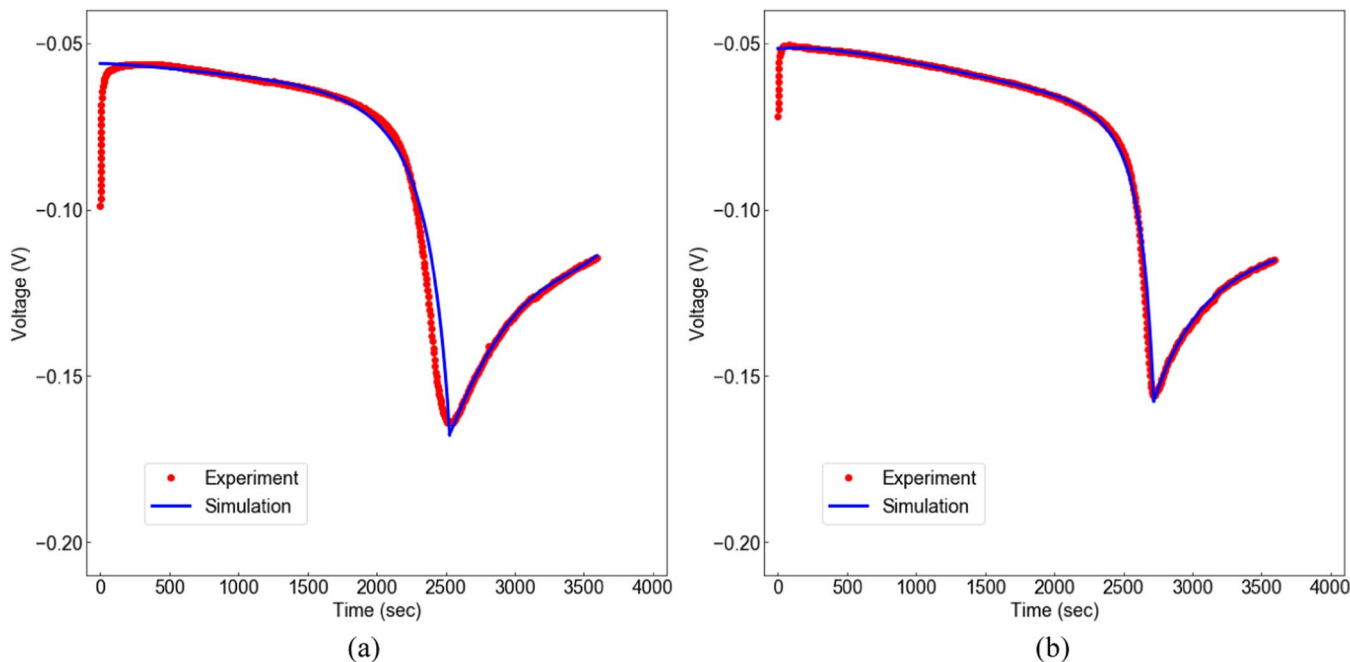


Figure 8. Comparison between model prediction and experimental voltage response for Phase 3(a) and Phase 5(b).

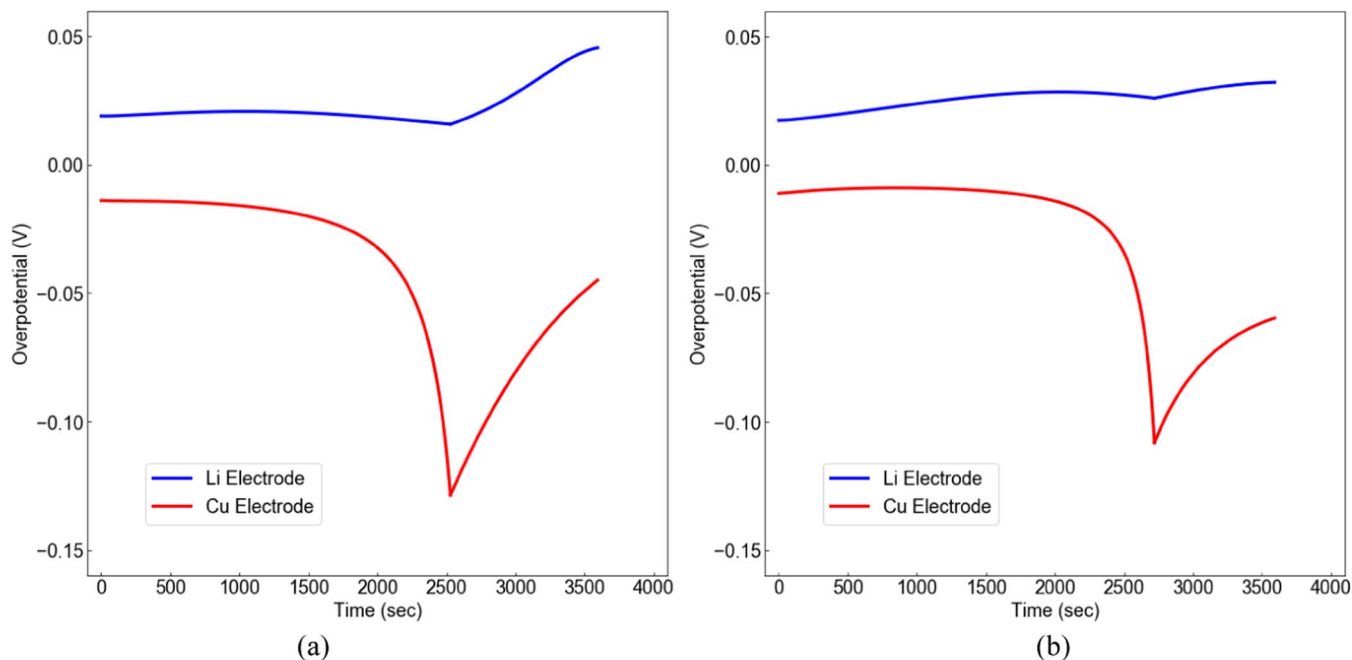


Figure 9. Simulated electrode overpotentials as a function of time for Phase 3(a) and Phase 5(b).

in effective exchange current densities, and this is borne out in the profiles of Figure 10, establishing the self-consistency of the model.

The above approach used an unconstrained approach which allowed the $i_{0,ref}(t)$ to vary freely within a physically acceptable range. We now consider a different mechanism for the observed voltage transition reported in literature. In particular, the exhaustion of kinetically fast deposits at the stripping electrodes has been reported as the dominant cause of the voltage transition of Phase 3, and nucleation events at the deposition electrodes are not observed.⁹ A gradual increase in polarization at the Cu electrode is expected due to continually reducing Li^+ concentration. In addition, the surface area of deposits is

expected to reduce as the initial deposits grow in size and eventually merge. This effect is expected to manifest in the gradual reduction of $i_{0,effc}$ with time. However, it is possible that the reduction in $i_{0,effc}$ due to the unavailability of the electrochemically deposited Li, with its substantially enhanced kinetics is more significant and has a greater contribution to the voltage drop. This mechanism may be expressed in the optimization problem formulation through an additional constraint on the reference exchange current density at the Cu electrode. We can specify that the reference exchange current density can only decrease with time. Mathematically, this is expressed as:

$$i_{j+1,c} \leq i_{j,c}; \quad j = 1 \dots 5 \quad [78]$$

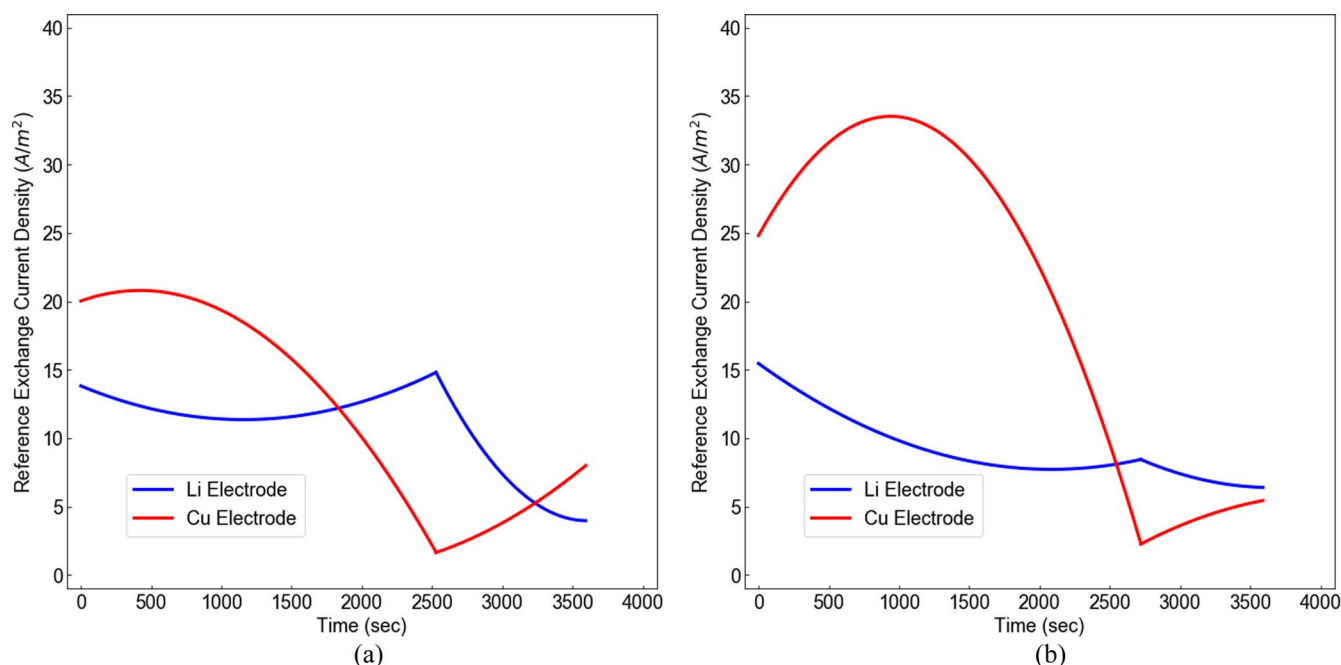


Figure 10. Temporal variation of the fitted reference exchange current density for Phase 3(a) and Phase 5(b).

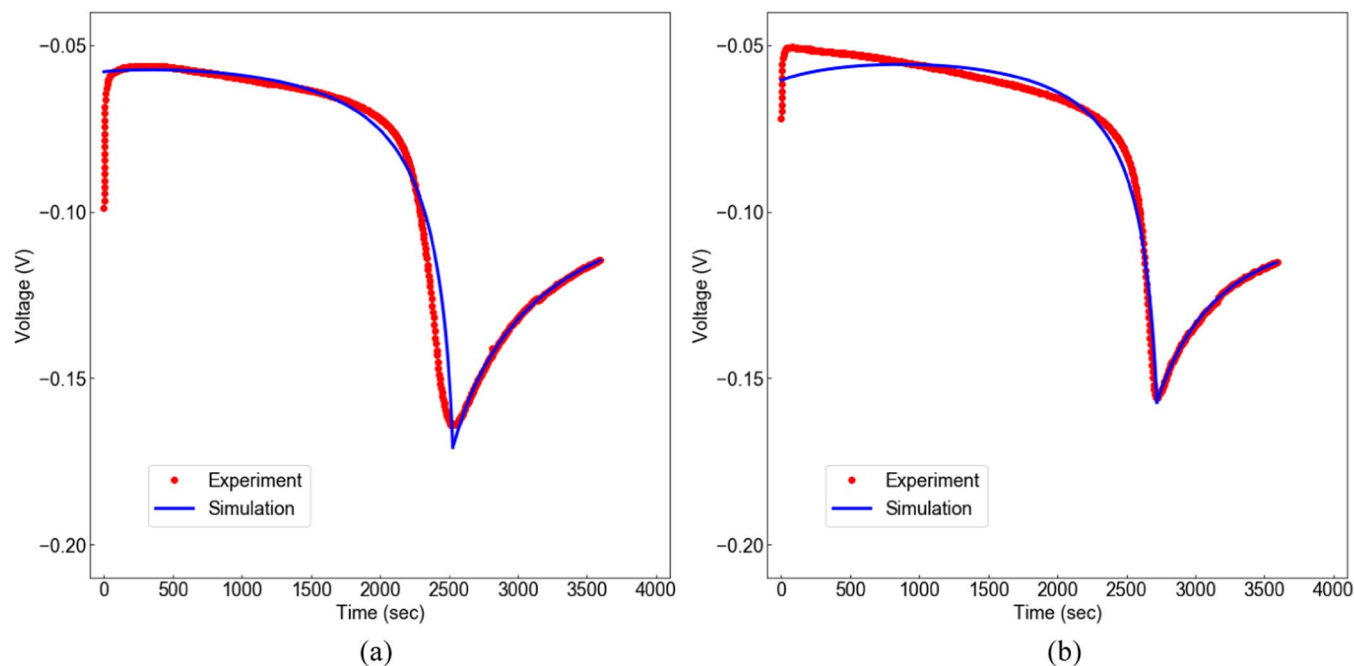


Figure 11. Comparison between model prediction and experimental voltage response for Phase 3(a) and Phase 5(b) with constraints at Cu electrode.

Figure 11 shows the voltage profiles obtained for this constrained case and indicates reasonable agreement between simulation and experimental data. Despite the disagreement in the initial part of Phase 5, the voltage transition is adequately captured. Figure 12 shows the simulated temporal evolution of electrode overpotentials. In contrast to the profiles of Figure 10, the overpotential of Li electrode is a dominant cause of voltage drop, while the Cu electrode overpotential increases much more slowly. The MAE between the model and data is only marginally higher compared to the previous unconstrained case (~ 6 mV vs 5 mV).

The behavior of overpotential at both electrodes is a result of the dynamics of the reference exchange current densities, as shown in Figure 13. While the exchange current density at Cu electrode is almost

constant, the Li electrode shows the drop and recovery of exchange current density over time. The variation of the exchange current density is over 15 A/m^2 , and it results in the increase in overpotential in Figure 12. This result is consistent with the mechanism of transition from fast to slow stripping. The constrained optimization suggests that mechanisms reported previously for Li-Li symmetric cells are able to match the voltage signatures for the experimental cell considered here. A more detailed model of Li deposition on Cu surfaces will help identify the precise mechanism underlying the voltage transitions and better explain the trends in the estimated parameters.

The systems-level approach is thus able to predict the key signatures in voltage response and can potentially provide useful insights into the relationship between voltage response and internal

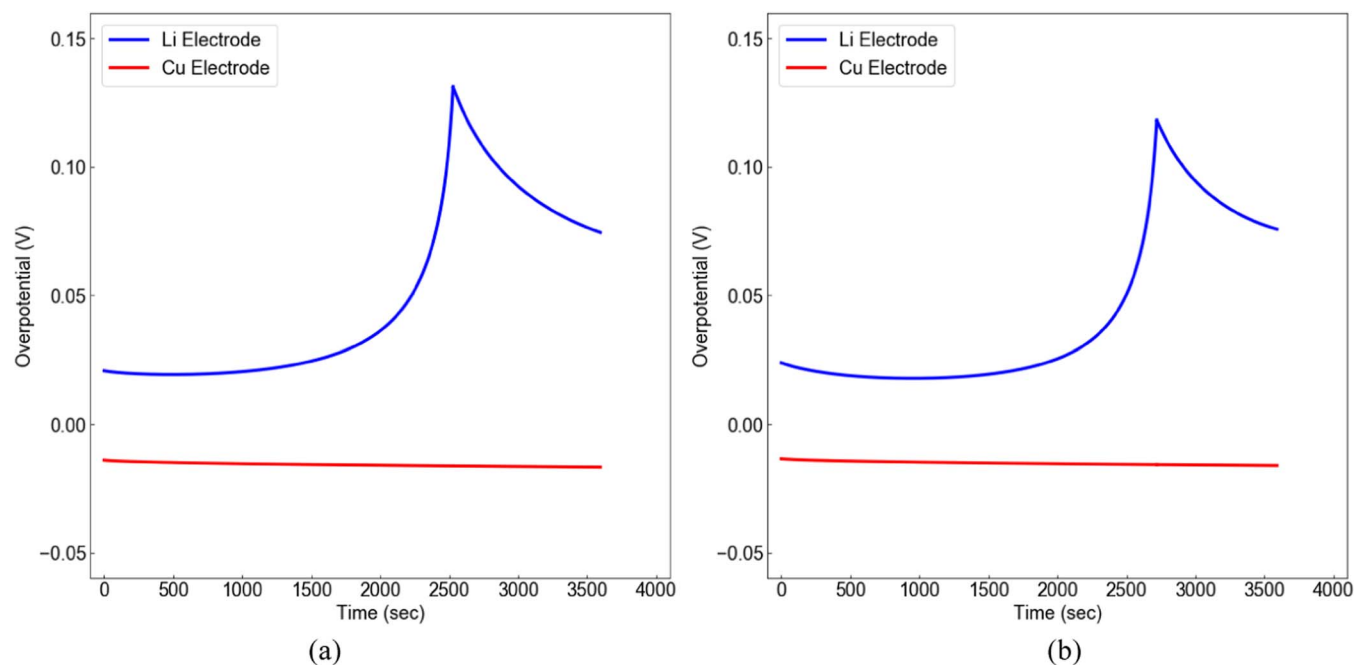


Figure 12. Simulated electrode overpotentials as a function of time for Phase 3(a) and Phase 5(b) with constraints at Cu electrode.

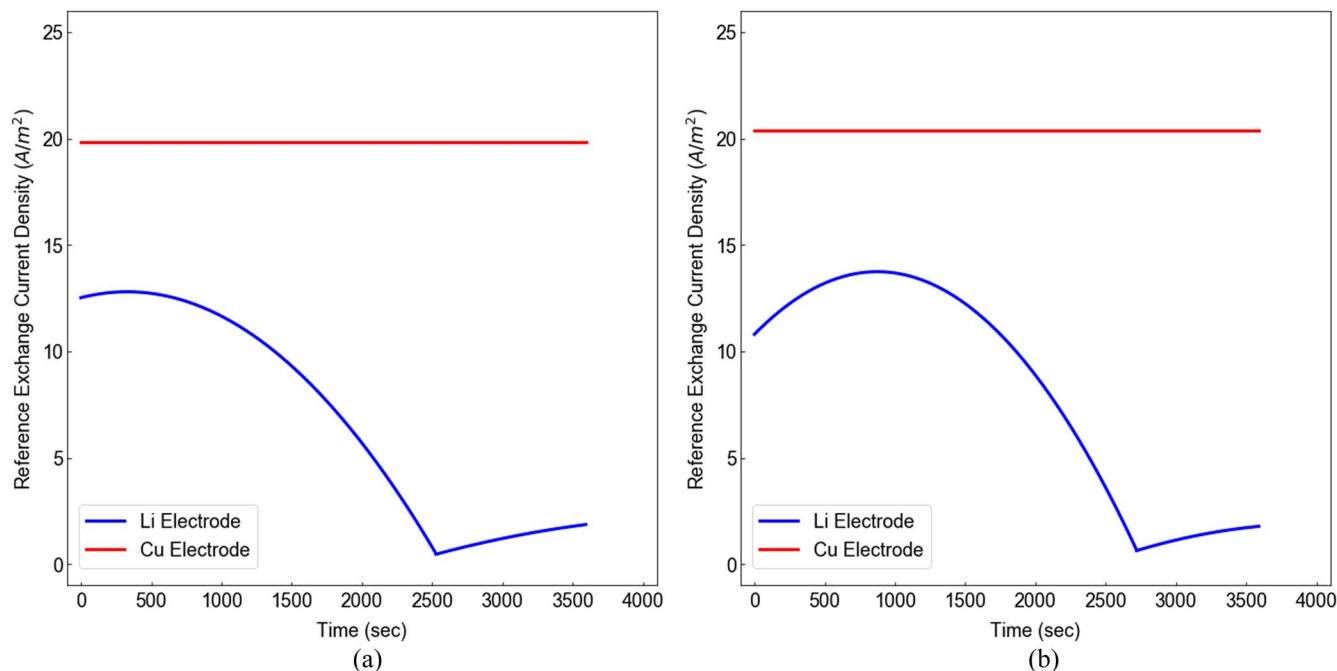


Figure 13. Temporal variation of the fitted reference exchange current density for Phase 3(a) and Phase 5(b) with constraints at Cu electrode.

electrochemistry. The analysis is substantially enabled by the fast transport model, which makes possible the simulation and parameterization over multiple cycles. The fast model opens up the possibility of testing different candidate mechanisms, expressed as equivalent profiles for $i_{0,ref}(t)$ for a range of systems and parameter combinations, reasonably informed by insights and physics as demonstrated in this section.

Code Dissemination

The approximate FVM implementation of the PNP model is available as executable code, soon to be hosted at the corresponding author's website (<http://sites.utexas.edu/maple>). The code may be used to simulate the spatiotemporal evolution of ion concentrations and electrostatic potentials in a symmetric cell under galvanostatic operation. The executable code runs the FVM model with $n = 1024$ node points. The adjustable parameters pertain to electrolyte concentrations, cell length, applied current density, diffusion coefficients, etc. described in Table IV. The code is provided without restrictions for academic use. Detailed information on the code and its usage will also be made available on the website. The simulation results may be combined with suitable electrode kinetics models to calculate cell-level voltage as a function of time, as demonstrated in this paper.

Conclusions

Transport models based on the Nernst-Planck (NP) flux laws were analyzed in the context of lithium symmetric cells. Both EN-NP and PNP models were considered for a binary electrolyte. The EN-NP model (with electroneutrality assumption) is found to capture the concentration and electrostatic potential dynamics reasonably well compared to the full PNP model, but a robust and efficient simulation algorithm is demonstrated for the PNP model. An analytical solution is reported for the EN-NP system. The validity of the model and the simulation approach in explaining the experimental behavior was examined by coupling the efficient transport models with electrode kinetics models and employing a systems-level parameterization approach to obtain time-dependent exchange current densities. This approach is able to achieve quantitative agreement with the transitions

in experimental voltage data, though the analysis suggests that more detailed physics are required to provide mechanistic explanations for the observed trends in estimated parameters. However, the fast transport model allows the quick evaluation of different candidate profiles by efficiently simulating the resulting voltage response, complementing experiments and helping achieve an improved understanding of lithium metal anodes.

Acknowledgments

The authors would like to express gratitude to Assistant Secretary for Energy Efficiency and Renewable Energy, Office of Vehicle Technologies of the DOE through the Advanced Battery Material Research (BMR) Program (Battery500 consortium), the Clean Energy Institute (CEI) at the University of Washington and the Washington Research Foundation (WRF) for partial monetary support of this work. N.R.G. acknowledges support by the Department of Defense (DoD) through the National Defense Science & Engineering Graduate Fellowship (NDSEG) Program.

Appendix

General analytical solutions for EN-NP.—For finding coefficient A_n for any cycle, we still follow the idea of Equation 34. The difference is that the initial dimensionless concentration is no longer uniform across the cell. The simplified $A_{n,j}$ (j^{th} galvanostatic cycle) can be expressed by the following recurrence relation:

$$A_{n,1} = \frac{\delta_1 (-1 + \cos(n\pi))}{n^2 \pi^2} \quad [\text{A1}]$$

$$A_{n,j+1} = A_{n,j} \exp(-n^2 \pi^2 \tau_j) + (\delta_{j+1} - \delta_j) \frac{\cos(n\pi) - 1}{n^2 \pi^2} \quad [\text{A2}]$$

The dimensionless concentration profile can be also expressed as:

$$C_j(X, \tau_j) = \left[\sum_{n=1}^{\infty} A_{n,j} \cos(n\pi X) \exp(-n^2 \pi^2 \tau_j) \right] - \frac{\delta_j}{2} X + 1 + \frac{\delta_j}{4} \quad [\text{A3}]$$

Obtaining electrostatic potential value at $x = 0$ by Gaussian quadrature.—If we are particularly interested in the potential at the boundaries rather than the profile across the cell, we can evaluate the potential at $x = 0$ (because we defined $\phi = 0$ at $x = L$) by Gaussian quadrature approximation. Table AI shows the results of using a different number of integration points at $x = 0$ using Gaussian-Legendre quadrature approximation. When

Table A1. The potential at $x = 0$ by Gaussian-Legendre approximation using different integration points.

m	$t = 1 \text{ s}$	$t = 6 \text{ s}$	$t = 36 \text{ s}$	$t = 100 \text{ s}$	$t = 3600 \text{ s}$
1	9.077964×10^{-4}	9.082839×10^{-4}	1.735120×10^{-3}	3.541051×10^{-3}	4.992880×10^{-3}
2	9.079289×10^{-4}	1.274546×10^{-3}	2.943894×10^{-3}	4.104423×10^{-3}	5.008643×10^{-3}
3	9.683264×10^{-4}	1.737706×10^{-3}	2.900398×10^{-3}	4.075433×10^{-3}	5.008683×10^{-3}
4	1.152398×10^{-3}	1.749635×10^{-3}	2.896741×10^{-3}	4.076097×10^{-3}	5.008683×10^{-3}
5	1.252632×10^{-3}	1.716824×10^{-3}	2.897312×10^{-3}	4.076087×10^{-3}	
6	1.263696×10^{-3}	1.718749×10^{-3}	2.897272×10^{-3}	4.076087×10^{-3}	
7	1.246675×10^{-3}	1.720205×10^{-3}	2.897274×10^{-3}		
8	1.237110×10^{-3}	1.719912×10^{-3}	2.897274×10^{-3}		
9	1.237268×10^{-3}	1.719905×10^{-3}			
10	1.239157×10^{-3}	1.719915×10^{-3}			
11	1.239606×10^{-3}	1.719914×10^{-3}			
12	1.239377×10^{-3}	1.719914×10^{-3}			
13	1.239263×10^{-3}				
14	1.239282×10^{-3}				
15	1.239301×10^{-3}				
16	1.239300×10^{-3}				
17	1.239297×10^{-3}				
18	1.239297×10^{-3}				

the operation time is longer, the profile is more linear (approach to steady-state), so fewer integration points are needed to achieve the designated accuracy.

Experimental Set-Up and Details: Li||Cu operando X-ray diffraction cell.—The experimental Li||Cu electrochemical cell, which enables us to quantify lithium metal using X-ray diffraction, is depicted in Figure A1. This is a modification of the cell used in Cao et al.³⁹ Copper is used as a working electrode instead of lithium foil to distinguish

between electrodeposited lithium and uncycled lithium. To allow the X-ray beam to pass through the cell, a Kapton window is used. The PEEK spring and frame ensure that the electrodes are well connected to the current collector screws and the active area is well defined. The lithium foil counter/reference electrode is intentionally designed to be slightly narrower than the cell width to allow bubbles to escape and the 1 M LiPF₆ in ethylene carbonate/dimethyl carbonate (EC/DMC) electrolyte is filled above the lithium counter electrode. Since this is an open cell design with no applied compression as in a typical coin cell, the electrochemical performance, including coulombic efficiencies, is suppressed.

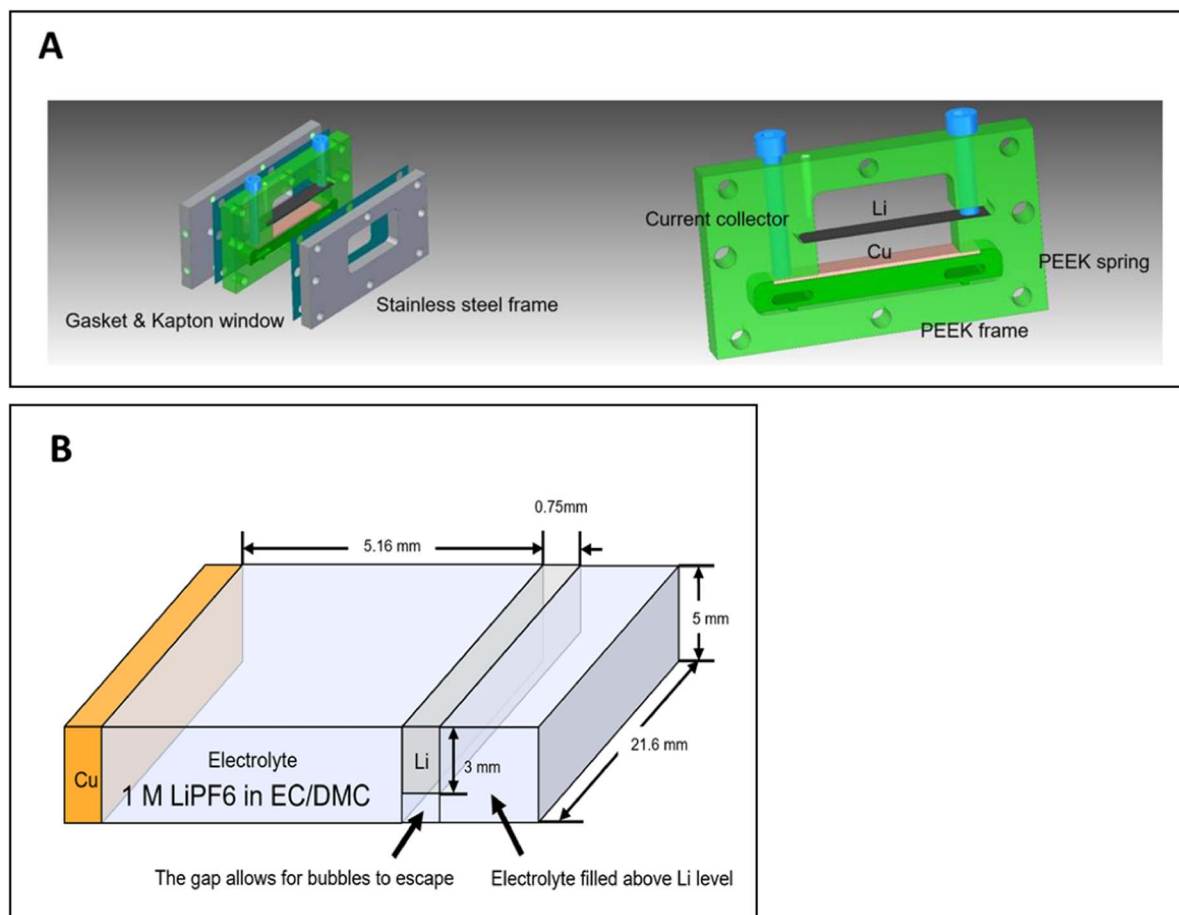


Figure A1. A: Diagram of the Li-Cu cell. B: A schematic representation indicating relevant dimensions of the electrode and electrolyte region.

ORCID

Jerry Chen  <https://orcid.org/0000-0003-0999-6644>
 Robert M. Kasse  <https://orcid.org/0000-0003-0738-744X>
 Michael F. Toney  <https://orcid.org/0000-0002-7513-1166>
 Venkat R. Subramanian  <https://orcid.org/0000-0002-2092-9744>

References

1. P. Albertus, S. Babinec, S. Litzelman, and A. Newman, *Nat. Energy*, **3**, 16 (2018).
2. J. Qian, W. A. Henderson, W. Xu, P. Bhattacharya, M. Engelhard, O. Borodin, and J. G. Zhang, *Nat. Commun.*, **6**, 6362 (2015).
3. M. D. Tikekar, S. Choudhury, Z. Tu, and L. A. Archer, *Nat. Energy*, **1**, 16114 (2016).
4. D. Lin, Y. Liu, and Y. Cui, *Nat. Nanotechnol.*, **12**, 194 (2017).
5. K. N. Wood, M. Noked, and N. P. Dasgupta, *ACS Energy Lett.*, **2**, 664 (2017).
6. J. C. Burns, L. J. Krause, D.-B. Le, L. D. Jensen, A. J. Smith, D. Xiong, and J. R. Dahn, *J. Electrochem. Soc.*, **158**, A1417 (2011).
7. D. M. Pesko, Z. Feng, S. Sawhney, J. Newman, V. Srinivasan, and N. P. Balsara, *J. Electrochem. Soc.*, **165**, A3186 (2018).
8. S.-L. Wu, A. E. Javier, D. Devaux, N. P. Balsara, and V. Srinivasan, *J. Electrochem. Soc.*, **161**, A1836 (2014).
9. K. N. Wood, E. Kazyak, A. F. Chadwick, K. H. Chen, J. G. Zhang, K. Thornton, and N. P. Dasgupta, *ACS Cent. Sci.*, **2**, 790 (2016).
10. H. Cohen and J. W. Cooley, *Biophys. J.*, **5**, 145 (1965).
11. T. R. Brumleve and R. P. Buck, *J. Electroanal. Chem.*, **90**, 1 (1978).
12. I. Streeter and R. G. Compton, *J. Phys. Chem. C*, **112**, 13716 (2008).
13. T. Sokalski, P. Lingelfelter, and A. Lewenstam, *J. Phys. Chem. B*, **107**, 2443 (2003).
14. D. Britz and J. Strutwolf, *Electrochim. Acta*, **137**, 328 (2014).
15. M. Z. Bazant, K. Thornton, and A. Ajdari, *Phys. Rev. E - Stat. Physics, Plasmas, Fluids, Relat. Interdiscip. Top.*, **70**, 021506 (2004).
16. A. F. Chadwick, G. Vardar, S. DeWitt, A. E. S. Sleightholme, C. W. Monroe, D. J. Siegel, and K. Thornton, *J. Electrochem. Soc.*, **163**, A1813 (2016).
17. K. T. Chu and M. Z. Bazant, *SIAM J. Appl. Math.*, **65**, 1485 (2005).
18. E. J. F. Dickinson and R. G. Compton, *Chem. Phys. Lett.*, **497**, 178 (2010).
19. A. Golovnev and S. Trimper, *J. Chem. Phys.*, **134**, 154902 (2011).
20. M. Pabst, *J. Chem. Phys.*, **140**, 224113 (2014).
21. M. Doyle, T. J. Fuller, and J. Newman, *J. Electrochem. Soc.*, **140**, 1526 (1993).
22. J. Newman and K. E. Thomas-Alyea, *Electrochemical Systems*, 3rd ed., John Wiley & Sons, Inc., Hoboken, NJ (2004).
23. A. M. Bizeray, D. A. Howey, and C. W. Monroe, *J. Electrochem. Soc.*, **163**, E223 (2016).
24. Z. Song, X. Cao, and H. Huang, *Phys. Rev. E*, **97**, 012411 (2018).
25. E. J. F. Dickinson, J. G. Limon-Petersen, and R. G. Compton, *J. Solid State Electrochem.*, **15**, 1335 (2011).
26. V. G. Levich, *Physicochemical Hydrodynamics*, Prentice-Hall, Englewood Cliffs, NJ (1962).
27. T. R. Rosebrugh and W. L. Miller, *J. Phys. Chem.*, **14**, 816 (1910).
28. R. E. White and V. R. Subramanian, *Computational Methods in Chemical Engineering with Maple*, Springer-Verlag, Berlin (2010).
29. M. Torchio, L. Magni, R. B. Gopaluni, R. D. Braatz, and D. M. Raimondo, *J. Electrochem. Soc.*, **163**, A1192 (2016).
30. Y. Zeng, P. Albertus, R. Klein, N. Chaturvedi, A. Kojic, M. Z. Bazant, and J. Christensen, *J. Electrochem. Soc.*, **160**, A1565 (2013).
31. V. R. Subramanian, V. Boovaragavan, V. Ramadesigan, and M. Arabandi, *J. Electrochem. Soc.*, **156**, 260 (2009).
32. A. Subramaniam, J. Chen, and V. R. Subramanian, *Meet. Abstr.*, **MA2018-02**, 520 (2018).
33. V. Ramadesigan, P. W. C. Northrop, S. De, S. Santhanagopalan, R. D. Braatz, and V. R. Subramanian, *J. Electrochem. Soc.*, **159**, R31 (2012).
34. P. W. C. Northrop, B. Suthar, V. Ramadesigan, S. Santhanagopalan, R. D. Braatz, and V. R. Subramanian, *J. Electrochem. Soc.*, **161**, E3149 (2014).
35. G. F. Carey and B. A. Finlayson, *Chem. Eng. Sci.*, **30**, 587 (1974).
36. A. C. Hindmarsh, R. Serban, and A. Collier, *Cent. Appl. Sci. Comput. LLNL* (2018).
37. E. Hairer and G. Wanner, *Solving Ordinary Differential Equations II: Stiff and Differential-Algebraic Problems*, Springer-Verlag, Berlin (1996).
38. C. Monroe and J. Newman, *J. Electrochem. Soc.*, **150**, A1377 (2003).
39. C. Cao, H. G. Steinrück, B. Shyam, K. H. Stone, and M. F. Toney, *Nano Lett.*, **16**, 7394 (2016).